

MedIL: Implicit Latent Spaces for Generating Heterogeneous Medical Images at Arbitrary Resolutions

Tyler Spears 

Shen Zhu 

Yinzhu Jin 

Aman Shrivastava

P. Thomas Fletcher 

TAS6HH@VIRGINIA.EDU

SZ9JT@VIRGINIA.EDU

YJ3CZ@VIRGINIA.EDU

AS3EK@VIRGINIA.EDU

PTF8V@VIRGINIA.EDU

Dept. of Electrical & Computer Engineering, University of Virginia, Charlottesville, VA, USA

Abstract

In this work, we introduce MedIL, a first-of-its-kind autoencoder built for encoding medical images with heterogeneous sizes and resolutions for image generation. Medical images are often large and heterogeneous, where fine details are of vital clinical importance. Image properties change drastically when considering acquisition equipment, patient demographics, and pathology, making realistic medical image generation challenging. Recent work in latent diffusion models (LDMs) has shown success in generating images resampled to a fixed-size. However, this is a narrow subset of the resolutions native to image acquisition, and resampling discards fine anatomical details. MedIL utilizes implicit neural representations to treat images as continuous signals, where encoding and decoding can be performed at arbitrary resolutions without prior resampling. We quantitatively and qualitatively show how MedIL compresses and preserves clinically-relevant features over large multi-site, multi-resolution datasets of both T1w brain MRIs and lung CTs. We further demonstrate how MedIL can influence the quality of images generated with a diffusion model, and discuss how MedIL can enhance generative models to resemble raw clinical acquisitions.

Keywords: LDM, autoencoder, INR

1. Introduction

Medical images come in all shapes and sizes. For example, a T1w magnetic resonance image (MRI) of the brain has a spatial resolution dependent upon scan sequence, magnetic field strength, etc. Similarly, lung computational tomography (CT) images may be acquired with different out-of-plane resolutions ([Armato III et al., 2015](#)). These parameters further depend on the pathology of interest, the quality of scanner hardware, and other external factors. This diversity of image resolutions poses a challenge for generative models that aim to learn a distribution of medical images. If such models are to fully represent real-world clinical images, anatomical details must be preserved throughout the model.

Recent denoising diffusion probability models (DDPM) are more tractable when trained on a compressed latent space, with an accompanying autoencoder, in a latent diffusion model (LDM). This reliance on compression implies that the generative power of an LDM is only as good as its autoencoder. However, most LDM autoencoders require a fixed input size to produce a fixed latent space shape, which further requires input data to be resampled and manipulated. Thus, the limitations of these autoencoders require image homogenization, which narrows image diversity and hinders the DDPM from the start.

To resolve this bottleneck, we introduce MedIL - **M**edical images from **I**mplicit **L**atent spaces. MedIL is a novel autoencoder that utilizes implicit neural representations (INRs) to flexibly encode medical images *without any prior resampling*. The INRs used in MedIL consider images as discrete samples of 3D spatially-continuous signals with physical coordinates, which allows for sampling at any arbitrary coordinate. This flexibility enables MedIL to encode any resolution of medical images, produce latent spaces of any size, and decode latent space samples to any arbitrary resolution. Our contributions are as follows:

- We propose and describe MedIL, a novel autoencoder built for encoding and decoding medical images with heterogeneous resolutions.
- We demonstrate MedIL as an autoencoder for T1w brain MRIs and lung CTs.
- We show how MedIL’s flexibility improves downstream generative image tasks.
- We publicly release our MedIL implementation which includes model implementations and utility functions for future work in spatially-continuous autoencoders. (<https://github.com/TylerSpears/medil>)

2. Background

2.1. Related Work

Deep generative models for medical images have been applied to a variety of imaging tasks for several years. More recently, these models have been improved with the denoising diffusion probabilistic model (DDPM) (Ho et al., 2020). Authors in (Dorjsembe et al., 2022) were one of the first to demonstrate unconditional generation of 3D T1w brain MRIs using a DDPM, with subsequent work (Pinaya et al., 2022) improving image quality. The more specific problem of arbitrary-resolution image generation is a sub-field of image generation where the source and/or target distributions do not have a fixed size. Many arbitrary-resolution works use generative adversarial networks (GANs) enhanced with positional encoding. INR-GAN was proposed by (Skorokhodov et al., 2021), which used a hypernetwork to produce the weights of a per-image INR. Authors in (Ntavelis et al., 2022) utilized positional encodings and scale-consistency to generate partial images. Anyres-GAN (Chai et al., 2022) generated nature images of varying aspect ratios using a GAN with pixel coordinates. There are few works in this sub-field with DDPMs, and to the best of our knowledge, there are no prior works on arbitrary-resolution medical image generation with DDPMs.

2.2. Latent Diffusion Models

Traditional diffusion models denoise Gaussian samples in pixel space, requiring intensive computation for high-resolution images and sequential sampling steps. Latent Diffusion Models (LDMs) (Rombach et al., 2022) address this by operating in compressed latent space. First, an autoencoder perceptually compresses inputs into a lower-dimensional latent space. Next, a diffusion model is trained in this latent representation, enabling scalable high-resolution synthesis. Building on standard diffusion models (Ho et al., 2020), LDMs (Rombach et al., 2022) implement diffusion in compressed latent space. The forward process gradually adds Gaussian noise via $q(x_t|x_{t-1}) = \mathcal{N}(\sqrt{1 - \beta_t}x_{t-1}, \beta_t\mathbf{I})$ over T steps, converging to

$\mathcal{N}(0, \mathbf{I})$. The reverse process learns to denoise through $p_\theta(x_{t-1}|x_t) = \mathcal{N}(\boldsymbol{\mu}_\theta(x_t, t), \boldsymbol{\Sigma}_\theta(x_t, t))$, trained using a hybrid loss (Nichol and Dhariwal, 2021) (where ϵ_θ predicts the added noise):

$$L_{\text{hybrid}} = \underbrace{\mathbb{E}_{t,x_0,\epsilon} \|\epsilon - \epsilon_\theta(x_t, t)\|^2}_{L_{\text{simple}}} + \lambda \underbrace{L_{\text{vlb}}}_{\text{VLB objective}} \quad (1)$$

2.3. Continuous Image Representations with INRs

INRs are MLPs that learn a continuously-valued representation of a discretely-sampled signal. While many INRs learn to represent a single image or scene, such as neural radiance fields (NeRF) and sinusoidal representation networks (SIREN) (Mildenhall et al., 2021; Sitzmann et al., 2020), other methods consider INRs as a learned interpolation kernel over space. For example, the Local Implicit Image Function (LIIF) is an arbitrary-size super-resolution method for upsampling images to any zoom factor (Chen et al., 2021).

For notational consistency, let us define $\Omega \subset \mathbb{R}^d$ as a continuous, bounded coordinate space which contains the coordinates of all images in our dataset. Also, denote variables $C \subset \Omega$ as discrete, rectilinear grids of coordinate vectors $c \in C$ (thus, $c \in \mathbb{R}^d$). Then, LIIF considers every pixel x in image X as a discrete sample with an associated coordinate $c_X \in C_X$, where $d = 2$ for 2D images¹. The output of LIIF is determined by a query coordinate $c_Q \in C_Q$ that can be calculated by a transformation of c_X , e.g. zoom. LIIF uses an MLP f_θ to create a function $F(f_\theta, X, C_X, C_Q)$ that reconstructs the image X at coordinates C_Q .

To avoid grid artifacts at pixel boundaries, LIIF performs 4 forward-passes at each nearest-neighbor point (the local “ensemble”) in C_X relative to every c_Q . Denote the coordinate $c_X^{i,j}$ with $i, j \in \{0, 1\}$, as the coordinate in C_X that is the (i, j) th nearest pixel to a c_Q , and let $X[c_X]$ be a sampling operation of X at c_X . Then, the INR forward passes are linearly combined as

$$F(f_\theta, X, C_X, c_Q) = \sum_i \sum_j w^{i,j} f_\theta \left(X \left[c_X^{i,j} \right], c_X^{i,j}, c_Q \right), \quad (2)$$

where $w^{i,j}$ is the linear interpolation weight of the i, j ’th forward pass.

Subsequent INR works used positional encodings to reduce the spectral bias in INRs (Tancik et al., 2020; Xu et al., 2022). The local texture estimator (LTE) (Lee and Jin, 2022), used in MedIL, builds on LIIF by learning these positional encodings as frequencies and phase offsets for image super-resolution.

3. MedIL

MedIL is an autoencoder architecture where all volumes are treated as a sample of a spatially-continuous signal using a mix of convolutional and INR modules in both the encoder and decoder. The MedIL architecture is illustrated in Figure 1. The input, latent, and output volumes (X , Z , and \hat{X} , respectively) all have associated coordinate grids C_X , C_Z , and $C_{\hat{X}}$ which are contained in the bounded, continuous coordinate space Ω . Medical

1. We constrain our notation to 2D in describing previous work, but our MedIL implementation is in 3D.

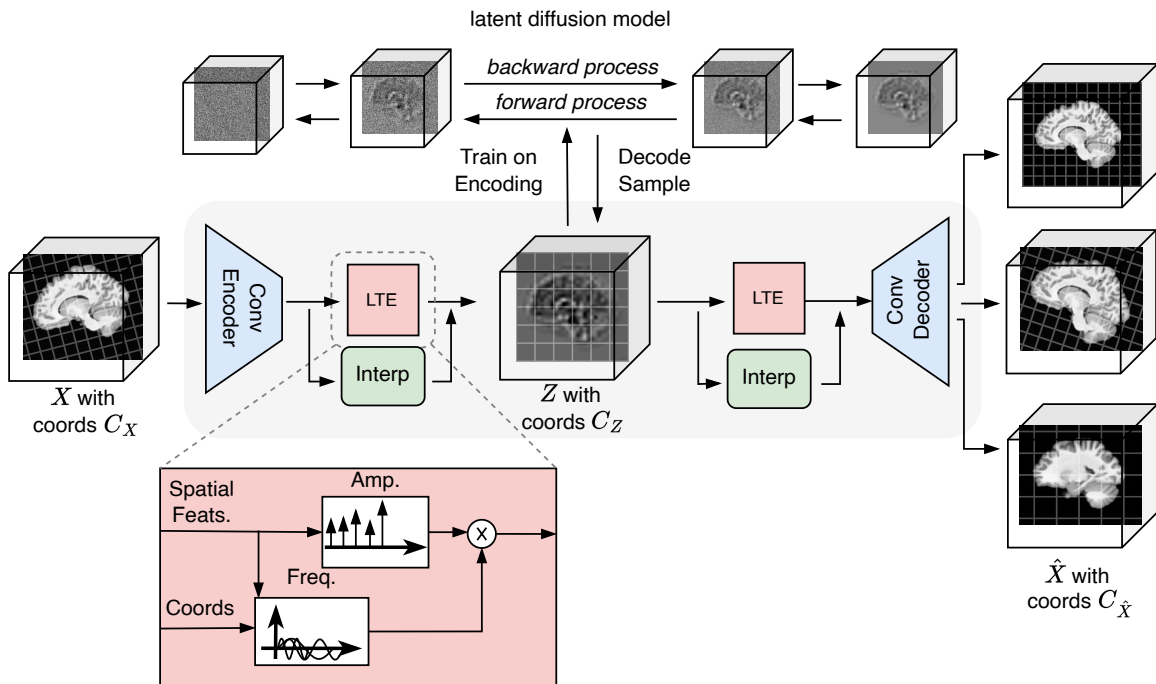


Figure 1: MedIL architecture. Input volumes X are encoded into latent volumes Z , which can then be decoded to arbitrary output resolutions or orientations.

images are unique in that voxel locations have defined physical coordinates, so Ω may be defined by the scanner’s field of view (FoV) or a template space (Evans et al., 1993). We then consider encoding as a transformation of X into the Z via their coordinate grids C_X and C_Z . Similarly, decoding is a transformation of Z to \hat{X} using a coordinate transformation from C_Z to $C_{\hat{X}}$. As illustrated in Figure 1, MedIL is capable of decoding (and encoding) images of arbitrary resolution and orientation so long as their coordinates are contained within Ω . This flexibility allow MedIL to encode fixed-size, but feature-rich, latent representations for subsequent image generation tasks.

The MedIL encoder comprises a fully convolutional backbone and an LTE network. This backbone encodes spatial context for the sampling module and spatially compresses X by some integer factor(s). This helps “spread out” the compression burden between layers, and reduces the memory requirements for a 3D LTE. The LTE module then continuously resamples the convolutional backbone’s output to the coordinates C_Z , producing Z . The decoder must then resample Z into \hat{X} via C_Z and $C_{\hat{X}}$. The decoder mirrors the encoder, starting with an LTE module to perform the “variable” resampling, and a convolutional backbone to upsample by an integer factor.

Training with Large Volumes. Due to the large size of raw medical images (i.e. 512^3 voxels), it is infeasible to train MedIL over entire volumes. So, based on work in (Chai et al., 2022), we break up training MedIL into two stages. First, we pretrain MedIL on

volumes downsampled to a standard size such that features across the entire FoV of Ω are available to MedIL. Second, patches of full-resolution volumes are randomly sampled from a tissue mask. These \hat{X} volumes have a fixed *voxel* shape, but their *physical* resolutions may vary. We also ensure spatial context around \hat{X} by selecting C_Z such that the boundary points of C_Z encompass $C_{\hat{X}}$ with some buffer space. We similarly “exscribe” C_X around C_Z .

4. Experiments & Results

4.1. Data

T1w Brain MRIs. To maximize the diversity of acquisition sites and image parameters, we chose to train MedIL on T1w brain MRIs from five different publicly available datasets: the Young Adult Human Connectome Project (HCP) (Van Essen et al., 2013), the Autism Brain Imaging Data Exchange (ABIDE) 1 and 2 (Di Martino et al., 2014, 2017), the Open Access Series of Imaging Studies-3 (OASIS3) dataset (LaMontagne et al., 2019), and the Center of Reproducible Research (CoRR) brain dataset (Zuo et al., 2014). We selected healthy adult (≥ 21 years of age) subjects with a total of roughly 3,700 unique subjects and slightly over 7,000 volumes, as various datasets provided multiple scans per subject.

Lung CTs. We further validated MedIL on a second image modality, CT images of lungs from the Lung Image Database Consortium and Image Database Resource Initiative (LIDC-IDRI) (Armato III et al., 2015). The LIDC-IDRI dataset consists of 1,000 lung CTs with out-of-plane resolutions ranging between 0.7mm to 5.0mm. Details are given in Appendix A.1, but we emphasize that no spatial interpolation was performed during preprocessing.

4.2. Comparison Models

We sought to compare MedIL to previously established fully-convolutional autoencoders found in the medical image literature. For the T1w brain MRIs, we recreated the LDM (both autoencoder and diffusion model) architecture and training parameters from (Pinaya et al., 2022). We similarly followed (Khader et al., 2023) for constructing and training an LDM for chest CTs. These models, which we name as Conv. LDMs, are built for fixed-size images, and we aim to reconstruct volumes at their native resolutions. So, we must first train these models on fixed-size volumes, then interpolate their output to the image’s native resolution. We resampled all T1w brain MRIs to be AC-PC aligned, with a 1mm isotropic resolution and size $160 \times 224 \times 160$. We also resampled all lung CTs to a resolution of 2.5mm isotropic with the shape 128^3 . These resampled data formed the training set for both the Conv. LDMs and the MedIL pretraining stage. We also compared MedIL to an ablation variant with the LTE module stripped out and replaced with only trilinear interpolation, which we name MedIL-Interp.

4.3. Experiment 1. Autoencoder Reconstruction of T1w Brain MRIs

In our first experiment, we evaluated MedIL’s reconstruction performance for native-resolution T1w brain MRIs. We compared MedIL to a Conv. LDM (Pinaya et al., 2022) with trilinear resampling into the native space. The latent space consisted of 3 channels, and its

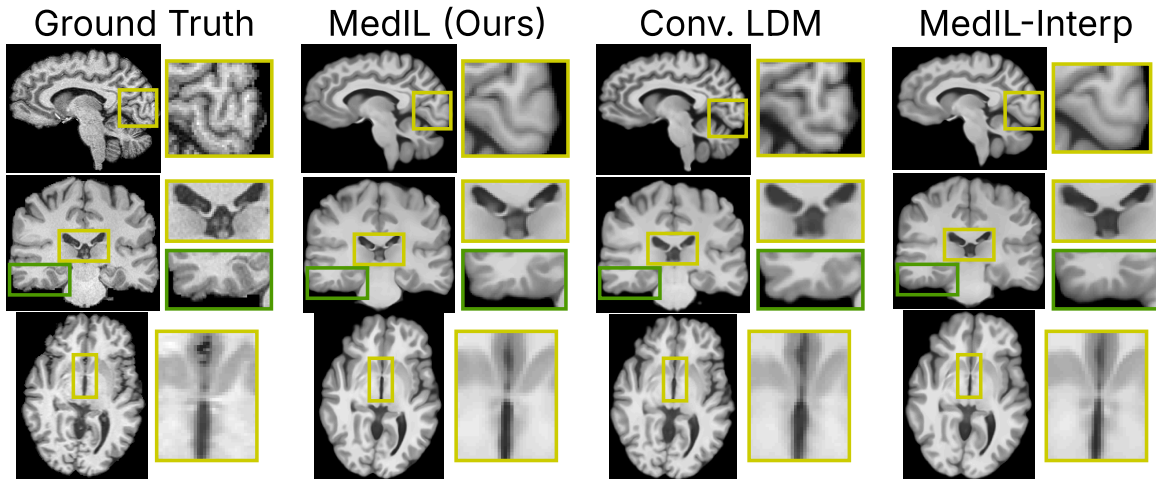


Figure 2: Reconstruction of real, native-space T1w brain MRIs.

Table 1: Results for reconstructing native-space T1w Brain MRIs (Experiment 1) and native-space lung CTs (Experiment 2). All images were scaled to the range $[0, 1]$.

	$\downarrow \ell_1$	\uparrow PSNR	\uparrow SSIM	\uparrow MS-SSIM	\downarrow Perceptual
<i>Experiment 1: Brain MRI</i>					
Conv. LDM	0.035424	30.188066	0.879466	0.975497	0.000183
MedIL-Interp (Ablation)	0.041470	29.222708	0.846165	0.959142	0.000375
MedIL (Ours)	0.037323	30.040161	0.868112	0.969519	0.000302
<i>Experiment 2: Lung CT</i>					
Conv. LDM	0.026827	32.547900	0.827005	0.955557	0.003036
MedIL-Interp (Ablation)	0.030542	31.815599	0.833598	0.949818	0.000913
MedIL (Ours)	0.027418	32.770102	0.851286	0.959340	0.000779

coordinate grid C_Z was AC-PC aligned with 8mm spacing. Test sets consisted of 50 randomly selected subjects per dataset, giving 250 test volumes. Model reconstructions were evaluated by ℓ_1 , peak signal-to-noise ratio (PSNR), the structural similarity index measure (SSIM) (Wang et al., 2004), multi-scale SSIM (Wang et al., 2003), and the Med3D learned perceptual metric (Chen et al., 2019).

Reconstructions examples for Experiment 1 are shown in Figure 2, and quantitative results are shown in Table 1. MedIL produces high-quality reconstructions of native-resolution T1w brain MRIs across multiple datasets. Even with resolutions as high as 0.7mm, greater than a $10\times$ downsampling to Z , MedIL preserves small details. Row 1 highlights how MedIL can maintain the separation of gyri, whereas Conv. LDMs may struggle (though the opposite may often occur). The gold boxes in Figure 2 rows 2 and 3 show how fine anatomical features are lost in the resampling required for Conv. LDMs, such as the boundary between the fornix and the Thalamus. In row 3, the inferior edge of the anterior commissure is disconnected for Conv. LDM, but maintained by MedIL. These results also demonstrate

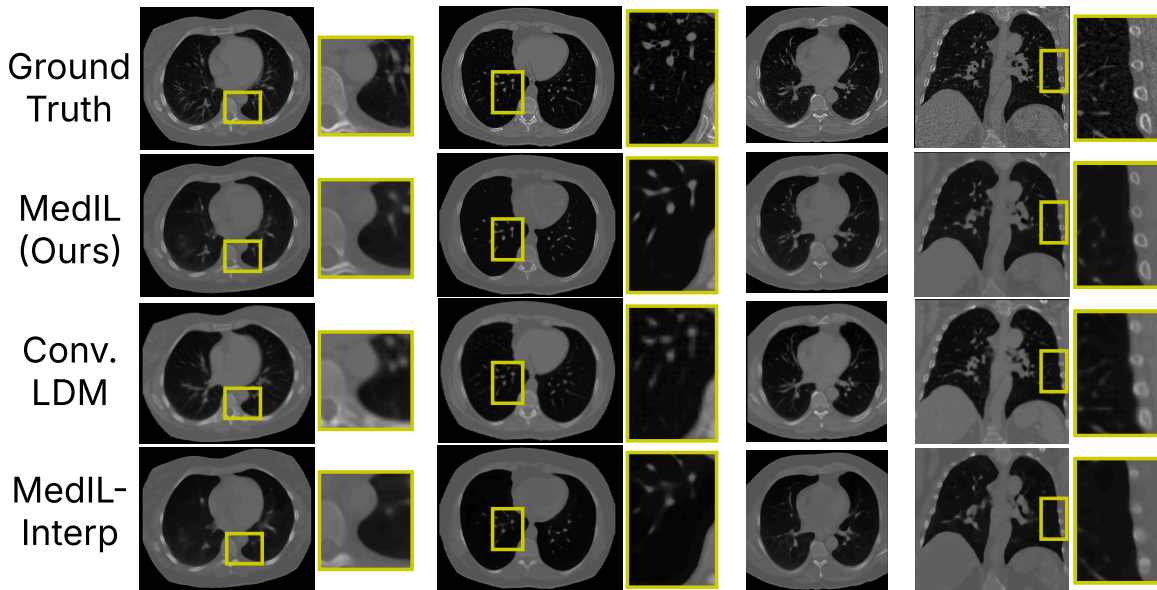


Figure 3: Reconstruction of real, native-space lung CTs.

some weaknesses of MedIL, such as a less clear separation between white and gray matter. Additionally, we observed that at higher resolutions, MedIL may insert extraneous gyri as shown in the green boxes in row 2. We hypothesize this is an effect of the pretraining on 1mm data. For the quantitative results in Table 1, MedIL is highly competitive with Conv. LDM in all tested metrics. MedIL also outperformed the ablation model in all given metrics, demonstrating the advantage of the learned resampling modules.

4.4. Experiment 2. Autoencoder Reconstruction of Lung CTs

In Experiment 2, we further validated MedIL as a general medical image autoencoder via reconstructing lung CTs at native resolutions. Unlike T1w brain MRIs, with resolutions between 0.7 to 1.3mm, the out-of-plane resolutions of lung CTs span 0.6 and 5mm for the LIDC-IDRI dataset. Furthermore, lung CTs may be extremely large (up to 512^3 voxels), posing a computational challenge when resampling cannot be performed. MedIL for lung CT was compared to the Conv. LDM described in (Khader et al., 2023). Following this previous work, Conv. LDM was trained on CTs from the LIDC-IDRI dataset resampled to 2.5mm isotropic (128 voxels). Evaluation was performed over a test set of 99 random subjects in the CT’s native resolution, with Conv. LDM reconstructions trilinearly resampled to the native resolution. Test performance metrics are the same as Experiment 1.

Example lung CT reconstructions are shown in Figure 3, and quantitative metrics are shown in Table 1. MedIL effectively reconstructs different tissue and bone boundaries over a range of CT resolutions. For example, in the left and right columns of Figure 3, MedIL maintains a clear border between tissue and air and even layers within bone. This is opposed to Conv. LDM where the necessary trilinear upsampling has blurred all boundaries. Inside the lungs, MedIL reconstructs the larger-scale nodules with clarity, but struggles with small,

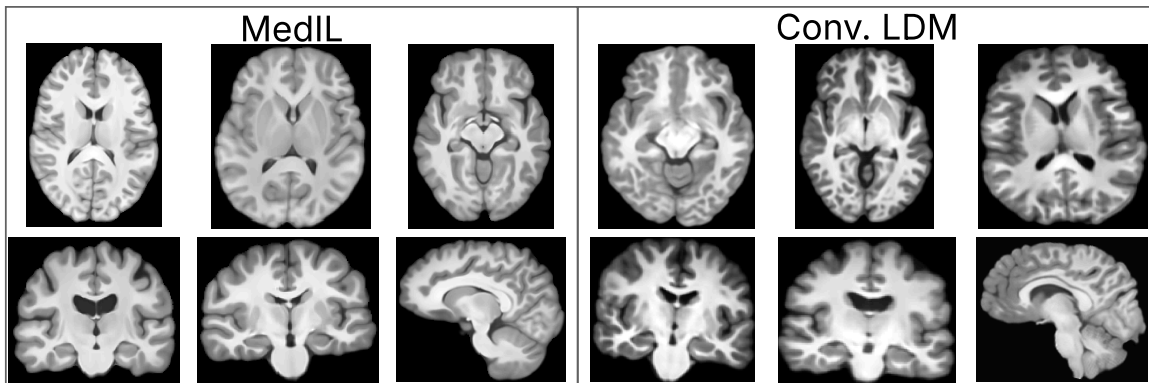


Figure 4: Example T1w MRIs generated with a DDPM on latent space samples.

Table 2: Generative model results for Experiment 3 trained with encodings from Experiments 1 and 2.

	↓ FID	↓ MS-SSIM	↑ Coverage		↑ Density	
			$k = 10$	$k = 30$	$k = 10$	$k = 30$
<i>Brain MRI</i>						
Conv. LDM	0.144	0.6903	0.556	0.856	0.131	0.1657
MedIL (Ours)	0.035	0.8090	0.675	0.888	0.2185	0.2857
Real Data	-	0.6801	-	-	-	-
<i>Lung CT</i>						
Conv. LDM	0.00769	0.4798	0.902	0.997	0.323	0.394
MedIL (Ours)	0.01410	0.4547	0.706	0.971	0.249	0.362
Real Data	-	0.4313	-	-	-	-

narrow branches, a clear example of the spectral bias problem (Tancik et al., 2020). Conv. LDM blurs and weakens these same branches, along with the nodules, but are not entirely erased. Despite this, MedIL quantitatively outperforms the comparison models in all metrics besides ℓ_1 . This performance is likely due to MedIL’s preservation of tissue boundaries, and each metric’s lower weighting of small, low-intensity bronchial features.

4.5. Experiment 3. Generating T1w Brain MRIs at Different Resolutions

In our final experiment, we sought to demonstrate how MedIL latent encodings may influence downstream image generation. Using the MedIL and Conv. LDM models from Experiments 1 and 2, we encoded the entire training and validation sets into latent samples and trained a UNet (Ronneberger et al., 2015) DDPM for 1,000 epochs. We sampled 1,000 latent volumes from the DDPM, and each model decoded its samples into 1mm AC-PC aligned space for the brain MRIs, and $0.7 \times 0.7 \times 2.5$ mm space for the lung CTs. For brain MRI, no resampling was required for Conv. LDM, and MedIL decoded samples into the 1mm output space with its decoder LTE. Whereas lung CT required resampling of the Conv.

LDM output using trilinear interpolation. We compared the synthetic and real data distributions multiple metrics including the Frechet Inception distance (FID) on Med3D (Chen et al., 2019), coverage, density (Naeem et al., 2020), and an MS-SSIM diversity metric. We also wanted to visualize synthetic T1w MRIs in native space. To emulate native spaces, we fit a Gaussian mixture model with 4 components to the resolutions and orientations found in the real data. We then sampled this transformation distribution for each DDPM sample, which became the output spaces. Finally, the DDPM samples were decoded into their respective output spaces.

The quantitative results of decoding samples to a fixed space are found in Table 2, and examples of the native-space decodings of brain MRIs are shown in Figure 4. For brain MRI, samples trained on MedIL encodings more closely match the real data distribution when compared to Conv. LDM on FID, coverage, and density, but had lower diversity according to MS-SSIM over 1,000 random pairs within each dataset. We hypothesize that this performance advantage may be due to MedIL’s sharper tissue boundaries (see Figure 4). In native-space decodings, qualitatively, we found that Conv. LDM often distorted small-scale anatomical features. In Figure 4, the top-left Conv. LDM sample shows a warped cerebral aqueduct, and the bottom-center shows a missing (or attenuated) fornix. This was not universal for Conv. LDM, but we did not see such distortions with MedIL. However, similar to the Experiment 1 results, MedIL did struggle to decode some samples into higher resolutions (roughly 0.8mm), producing unrealistic gyral topology. Overall, MedIL samples can be effectively decoded to many resolutions.

For generated lung CTs, we find that Conv. LDM more closely matches the real data distribution according to FID, coverage, and density, but MedIL has slightly better diversity according to MS-SSIM (over 200 random pairings within dataset). We hypothesize that, despite the higher reconstruction performance of MedIL in lung CTs, the features of importance in the Med3D network, which was used to estimate the feature distributions of each dataset, may prioritize bronchial tubes over bone, muscle, etc. These features would not be given preference by MS-SSIM.

4.6. Discussion

In this work, we introduced MedIL, a novel autoencoder architecture built for encoding medical images of all shapes and sizes. We have demonstrated MedIL’s capabilities for reconstructing medical images with different native spaces, for both T1w MRI and lung CT, and how MedIL’s flexible representations can improve fixed-size convolutional LDMs. However, this work is only an introduction of MedIL. Future work should focus on lowering the spectral bias found in many INRs, and expanding to conditional image generation to push towards generating clinical images with fine-scale, anatomically correct features.

Acknowledgments

We thank Dr. Miaomiao Zhang for insightful feedback and generously shared computational resources.

References

- Babak A. Ardekani and Alvin H. Bachman. Model-based automatic detection of the anterior and posterior commissures on MRI scans. *NeuroImage*, 46(3):677–682, July 2009. ISSN 1053-8119.
- Samuel G. Armato III, Geoffrey McLennan, Luc Bidaut, Michael F. McNitt-Gray, Charles R. Meyer, Anthony P. Reeves, Binsheng Zhao, Denise R. Aberle, Claudia I. Henschke, Eric A. Hoffman, Ella A. Kazerooni, Heber MacMahon, Edwin J.R. Van Beek, David Yankelevitz, Alberto M. Biancardi, Peyton H. Bland, Matthew S. Brown, Roger M. Engelmann, Gary E. Laderach, Daniel Max, Richard C. Pais, David P.Y. Qing, Rachael Y. Roberts, Amanda R. Smith, Adam Starkey, Poonam Batra, Philip Caligiuri, Ali Farooqi, Gregory W. Gladish, C. Matilda Jude, Reginald F. Munden, Iva Petkovska, Leslie E. Quint, Lawrence H. Schwartz, Baskaran Sundaram, Lori E. Dodd, Charles Fenimore, David Gur, Nicholas Petrick, John Freymann, Justin Kirby, Brian Hughes, Alessi Vande Castele, Sangeeta Gupte, Maha Sallam, Michael D. Heath, Michael H. Kuhn, Ekta Dharaiya, Richard Burns, David S. Fryd, Marcos Salganicoff, Vikram Anand, Uri Shreter, Stephen Vastagh, Barbara Y. Croft, and Laurence P. Clarke. Data From LIDC-IDRI, 2015.
- Lucy Chai, Michaël Gharbi, Eli Shechtman, Phillip Isola, and Richard Zhang. Any-Resolution Training for High-Resolution Image Synthesis. In Shai Avidan, Gabriel Brostow, Moustapha Cissé, Giovanni Maria Farinella, and Tal Hassner, editors, *Computer Vision – ECCV 2022*, pages 170–188, Cham, 2022. Springer Nature Switzerland. ISBN 978-3-031-19787-1.
- Sihong Chen, Kai Ma, and Yefeng Zheng. Med3D: Transfer Learning for 3D Medical Image Analysis, July 2019.
- Yinbo Chen, Sifei Liu, and Xiaolong Wang. Learning Continuous Image Representation with Local Implicit Image Function, April 2021.
- Anders M. Dale, Bruce Fischl, and Martin I. Sereno. Cortical Surface-Based Analysis: I. Segmentation and Surface Reconstruction. *NeuroImage*, 9(2):179–194, February 1999. ISSN 1053-8119.
- A. Di Martino, C.-G. Yan, Q. Li, E. Denio, F. X. Castellanos, K. Alaerts, J. S. Anderson, M. Assaf, S. Y. Bookheimer, M. Dapretto, B. Deen, S. Delmonte, I. Dinstein, B. Ertl-Wagner, D. A. Fair, L. Gallagher, D. P. Kennedy, C. L. Keown, C. Keyzers, J. E. Lainhart, C. Lord, B. Luna, V. Menon, N. J. Minshew, C. S. Monk, S. Mueller, R.-A. Müller, M. B. Nebel, J. T. Nigg, K. O’Hearn, K. A. Pelphrey, S. J. Peltier, J. D. Rudie, S. Sunaert, M. Thioux, J. M. Tyszka, L. Q. Uddin, J. S. Verhoeven, N. Wenderoth, J. L. Wiggins, S. H. Mostofsky, and M. P. Milham. The autism brain imaging data exchange: Towards

- a large-scale evaluation of the intrinsic brain architecture in autism. *Mol Psychiatry*, 19(6):659–667, June 2014. ISSN 1476-5578.
- Adriana Di Martino, David O’Connor, Bosi Chen, Kaat Alaerts, Jeffrey S. Anderson, Michal Assaf, Joshua H. Balsters, Leslie Baxter, Anita Beggiato, Sylvie Bernaerts, Laura M. E. Blanken, Susan Y. Bookheimer, B. Blair Braden, Lisa Byrge, F. Xavier Castellanos, Mirella Dapretto, Richard Delorme, Damien A. Fair, Inna Fishman, Jacqueline Fitzgerald, Louise Gallagher, R. Joanne Jao Keehn, Daniel P. Kennedy, Janet E. Lainhart, Beatriz Luna, Stewart H. Mostofsky, Ralph-Axel Müller, Mary Beth Nebel, Joel T. Nigg, Kirsten O’Hearn, Marjorie Solomon, Roberto Toro, Chandan J. Vaidya, Nicole Wenderoth, Tonya White, R. Cameron Craddock, Catherine Lord, Bennett Leventhal, and Michael P. Milham. Enhancing studies of the connectome in autism using the autism brain imaging data exchange II. *Sci Data*, 4(1):170010, March 2017. ISSN 2052-4463.
- Zolnamar Dorjsembe, Sodtavilan Odonchimed, and Furen Xiao. Three-Dimensional Medical Image Synthesis with Denoising Diffusion Probabilistic Models. In *Medical Imaging with Deep Learning*, April 2022.
- A.C. Evans, D.L. Collins, S.R. Mills, E.D. Brown, R.L. Kelly, and T.M. Peters. 3D statistical neuroanatomical models from 305 MRI volumes. In *1993 IEEE Conference Record Nuclear Science Symposium and Medical Imaging Conference*, pages 1813–1817 vol.3, October 1993.
- Jonathan Ho, Ajay Jain, and Pieter Abbeel. Denoising Diffusion Probabilistic Models, December 2020.
- Firas Khader, Gustav Müller-Franzes, Soroosh Tayebi Arasteh, Tianyu Han, Christoph Haarbuerger, Maximilian Schulze-Hagen, Philipp Schad, Sandy Engelhardt, Bettina Baeßler, Sebastian Foersch, Johannes Stegmaier, Christiane Kuhl, Sven Nebelung, Jakob Nikolas Kather, and Daniel Truhn. Denoising diffusion probabilistic models for 3D medical image generation. *Sci Rep*, 13(1):7303, May 2023. ISSN 2045-2322.
- Pamela J. LaMontagne, Tammie LS Benzinger, John C. Morris, Sarah Keefe, Russ Hornbeck, Chengjie Xiong, Elizabeth Grant, Jason Hassenstab, Krista Moulder, Andrei G. Vlassenko, Marcus E. Raichle, Carlos Cruchaga, and Daniel Marcus. OASIS-3: Longitudinal Neuroimaging, Clinical, and Cognitive Dataset for Normal Aging and Alzheimer Disease, December 2019. ISSN 1901-4902.
- Jaewon Lee and Kyong Hwan Jin. Local Texture Estimator for Implicit Representation Function. In *Proceedings of the IEEE/CVF Conference on Computer Vision and Pattern Recognition*, pages 1929–1938, 2022.
- Ilya Loshchilov and Frank Hutter. Decoupled Weight Decay Regularization, January 2019.
- Ben Mildenhall, Pratul P. Srinivasan, Matthew Tancik, Jonathan T. Barron, Ravi Ramamoorthi, and Ren Ng. NeRF: Representing scenes as neural radiance fields for view synthesis. *Commun. ACM*, 65(1):99–106, December 2021. ISSN 0001-0782.

- Muhammad Ferjad Naeem, Seong Joon Oh, Youngjung Uh, Yunjey Choi, and Jaejun Yoo. Reliable Fidelity and Diversity Metrics for Generative Models. In *Proceedings of the 37th International Conference on Machine Learning*, pages 7176–7185. PMLR, November 2020.
- Alex Nichol and Prafulla Dhariwal. Improved Denoising Diffusion Probabilistic Models, February 2021.
- Evangelos Ntavelis, Mohamad Shahbazi, Iason Kastanis, Radu Timofte, Martin Danelljan, and Luc Van Gool. Arbitrary-Scale Image Synthesis. In *2022 IEEE/CVF Conference on Computer Vision and Pattern Recognition (CVPR)*, pages 11523–11532, New Orleans, LA, USA, June 2022. IEEE. ISBN 978-1-6654-6946-3.
- Walter H. L. Pinaya, Petru-Daniel Tudosiu, Jessica Dafflon, Pedro F. Da Costa, Virginia Fernandez, Parashkev Nachev, Sebastien Ourselin, and M. Jorge Cardoso. Brain Imaging Generation with Latent Diffusion Models. In Anirban Mukhopadhyay, Ilkay Oksuz, Sandy Engelhardt, Dajiang Zhu, and Yixuan Yuan, editors, *Deep Generative Models*, pages 117–126, Cham, 2022. Springer Nature Switzerland. ISBN 978-3-031-18576-2.
- Robin Rombach, Andreas Blattmann, Dominik Lorenz, Patrick Esser, and Björn Ommer. High-Resolution Image Synthesis With Latent Diffusion Models. In *Proceedings of the IEEE/CVF Conference on Computer Vision and Pattern Recognition*, pages 10684–10695, 2022.
- Olaf Ronneberger, Philipp Fischer, and Thomas Brox. U-Net: Convolutional Networks for Biomedical Image Segmentation, May 2015.
- F. Ségonne, A. M. Dale, E. Busa, M. Glessner, D. Salat, H. K. Hahn, and B. Fischl. A hybrid approach to the skull stripping problem in MRI. *NeuroImage*, 22(3):1060–1075, July 2004. ISSN 1053-8119.
- Vincent Sitzmann, Julien N. P. Martel, Alexander W. Bergman, David B. Lindell, and Gordon Wetzstein. Implicit Neural Representations with Periodic Activation Functions, June 2020.
- Ivan Skorokhodov, Savva Ignatyev, and Mohamed Elhoseiny. Adversarial Generation of Continuous Images. In *Proceedings of the IEEE/CVF Conference on Computer Vision and Pattern Recognition*, pages 10753–10764, 2021.
- Matthew Tancik, Pratul P. Srinivasan, Ben Mildenhall, Sara Fridovich-Keil, Nithin Raghavan, Utkarsh Singhal, Ravi Ramamoorthi, Jonathan T. Barron, and Ren Ng. Fourier Features Let Networks Learn High Frequency Functions in Low Dimensional Domains, June 2020.
- Nicholas J. Tustison, Brian B. Avants, Philip A. Cook, Yuanjie Zheng, Alexander Egan, Paul A. Yushkevich, and James C. Gee. N4ITK: Improved N3 Bias Correction. *IEEE Transactions on Medical Imaging*, 29(6):1310–1320, June 2010. ISSN 1558-254X.

- David C. Van Essen, Stephen M. Smith, Deanna M. Barch, Timothy E. J. Behrens, Essa Yacoub, and Kamil Ugurbil. The WU-Minn Human Connectome Project: An overview. *NeuroImage*, 80:62–79, October 2013. ISSN 1053-8119.
- Z. Wang, E.P. Simoncelli, and A.C. Bovik. Multiscale structural similarity for image quality assessment. In *The Thirty-Seventh Asilomar Conference on Signals, Systems & Computers, 2003*, volume 2, pages 1398–1402 Vol.2, November 2003.
- Zhou Wang, A.C. Bovik, H.R. Sheikh, and E.P. Simoncelli. Image quality assessment: From error visibility to structural similarity. *IEEE TIP*, 13(4):600–612, April 2004. ISSN 1941-0042.
- Xingqian Xu, Zhangyang Wang, and Humphrey Shi. UltraSR: Spatial Encoding is a Missing Key for Implicit Image Function-based Arbitrary-Scale Super-Resolution, July 2022.
- Xi-Nian Zuo, Jeffrey S. Anderson, Pierre Bellec, Rasmus M. Birn, Bharat B. Biswal, Janusch Blautzik, John C. S. Breitner, Randy L. Buckner, Vince D. Calhoun, F. Xavier Castellanos, Antao Chen, Bing Chen, Jiangtao Chen, Xu Chen, Stanley J. Colcombe, William Courtney, R. Cameron Craddock, Adriana Di Martino, Hao-Ming Dong, Xiaolan Fu, Qiyong Gong, Krzysztof J. Gorgolewski, Ying Han, Ye He, Yong He, Erica Ho, Avram Holmes, Xiao-Hui Hou, Jeremy Huckins, Tianzi Jiang, Yi Jiang, William Kelley, Clare Kelly, Margaret King, Stephen M. LaConte, Janet E. Lainhart, Xu Lei, Hui-Jie Li, Kaiming Li, Kuncheng Li, Qixiang Lin, Dongqiang Liu, Jia Liu, Xun Liu, Yijun Liu, Guangming Lu, Jie Lu, Beatriz Luna, Jing Luo, Daniel Lurie, Ying Mao, Daniel S. Margulies, Andrew R. Mayer, Thomas Meindl, Mary E. Meyerand, Weizhi Nan, Jared A. Nielsen, David O’Connor, David Paulsen, Vivek Prabhakaran, Zhigang Qi, Jiang Qiu, Chunhong Shao, Zarrar Shehzad, Weijun Tang, Arno Villringer, Huiling Wang, Kai Wang, Dongtao Wei, Gao-Xia Wei, Xu-Chu Weng, Xuehai Wu, Ting Xu, Ning Yang, Zhi Yang, Yu-Feng Zang, Lei Zhang, Qinglin Zhang, Zhe Zhang, Zhiqiang Zhang, Ke Zhao, Zonglei Zhen, Yuan Zhou, Xing-Ting Zhu, and Michael P. Milham. An open science resource for establishing reliability and reproducibility in functional connectomics. *Sci Data*, 1(1):140049, December 2014. ISSN 2052-4463.

Appendix A. Experiment Details

For all experiments, one epoch corresponded to 200 batches of samples (whole volumes or patches), with an effective batch size of 8.

A.1. Data Preprocessing

T1w Brain MRI. Preprocessing of the T1w brain MRIs was performed on volumes in such a way as to focus the analysis on brain structures without compromising the high-frequency properties unique to each scan. The T1w scans were bias-corrected using N4ITK ([Tustison et al., 2010](#)) and skull-stripped with Freesurfer ([Dale et al., 1999](#); [Ségonne et al., 2004](#)). All brain MRIs were then aligned to a common orientation to account for head position in the scanner, which was performed using landmark detection of the anterior commissure-posterior commissure (AC-PC) plane with the `acpcdetect` tool ([Ardekani and Bachman,](#)

2009). We note that we only transformed the coordinate space such that each volume would be aligned in Ω , there was *no* resampling performed and all image content was kept its native resolution and orientation. Scans from HCP were excluded from this preprocessing as they were already preprocessed with specialized techniques at a high spatial resolution (0.7mm isotropic). Finally, each volume was scaled to a range of 0.0 to 1.0 such that the volume’s 99th percentile would have a value of 1.0.

Lung CT. Preprocessing of lung CTs followed the procedure described in (Khader et al., 2023) except that CT volumes were only cropped or padded to a common FoV rather than resampled. Transformations between X and the latent coordinates C_Z consisted only of scaling and translation with no rotation. Tissue masks were created by thresholding at -200 Hounsfield units (HUs), along with a morphological fill operation to include air in the lungs. Intensities were scaled such that the range $-1,000$ to $2,000$ HUs was mapped to $[0.0, 1.0]$.

A.2. Network Architectures

Experiment 1. MedIL’s convolutional backbone consisted of 4 residual blocks, all with kernel size 3, 2 residual units per block, and 2 subunits per residual unit. Channel sizes were 32, 64, 96, 96, and instance norm was used throughout the convolutional backbone. Downscaling factors were 2, 2, 1, with downsampling being performed with convolutions with strides > 1 . The convolutional layers in the decoder mirror those of the encoder, where upsampling is performed by nearest-neighbor interpolation. The LTE module operated on $k = 256$ frequency coefficients. The INR network was a 1-conv residual network with 256 internal channels, 3 residual blocks, 2 subunits per block, with instance normalization between each layer. The SiLU activation function was used, following (Pinaya et al., 2022). The Conv. LDM architecture also followed (Pinaya et al., 2022), including the structure of the convolutional network, and the objective function including terms for an ℓ_1 loss, a perceptual loss, an adversarial loss, and a KL latent space regularization term.

Experiment 2. MedIL’s convolutional backbone contained 3 residual blocks, kernel size 3, with 2 residual units per block, and 2 subunits per residual unit. Channel sizes were 32, 64, 96, and instance norm was used. Downscaling factors were 2, 2, with convolutional downsampling and upsampling being the same as in Experiment 1. The LTE module had $k = 192$ frequency coefficients. The INR was a residual network with 128 internal channels, 2 residual blocks, and 2 subunits per block. The SiLU activation function was also used.

The Conv. LDM architecture also followed (Khader et al., 2023). For the objective function, we kept the following terms from the previous work: ℓ_1 loss, adversarial loss, perceptual loss, and a KL regularization term. We did not include the codebook loss or the feature matching loss, but found it was not necessary as there was very high reconstruction performance from the Conv. LDM in Experiment 2.

A.3. Training Details

Experiment 1. MedIL was pre-trained on AC-PC aligned, 1mm isotropic data for 150 epochs. Then, both models were trained for 250 epochs with random patches of size $152 \times 184 \times 152$ on native-resolution data; an adversarial loss was used after epoch 125. Finally, the model decoder was fine-tuned for 50 epochs. MedIL used the AdamW (Loshchilov and

Hutter, 2019) optimizer with a base learning rate of 0.005, momentum of 0.9, $\beta_2 = 0.999$, and weight decay of 0.01. The Conv. LDM was trained for 300 epochs with an adversarial network used after 150 epochs. Checkpoints were selected by the ℓ_1 loss of a validation set of 8 subjects.

Training Time. Training times for each T1w autoencoder model are given below. Note that due to the time required to load and preprocess large volumetric data files, training time may vary according to the number of available CPU cores.

- Conv. LDM: 34 hours total on 4xA100 GPUs with 80 GB of GPU memory.
- MedIL: 22 hours for pretraining, 25 hours for full autoencoder training, and an additional 2 hours for decoder-only training for a total of 49 hours. MedIL was trained on 4xA100 GPUs with 80 GB of GPU memory.
- MedIL-Interp: 26 hours for pretraining, 29 hours for full autoencoder training, and an additional 4 hours for decoder-only training for a total of 59 hours. MedIL-Interp was trained on 4xA6000 with 48 GB of GPU memory.

Experiment 2. Conv. LDM was trained for 250 epochs, with an adversarial term used after 25 epochs. MedIL and MedIL-Interp were pretrained on the 2.5mm data for 150 epochs, then trained on native-space data for 125 epochs with no adversarial loss. The latent space had a resolution of 10mm isotropic, with only scaling and translation between the input X and latent volume Z . During MedIL’s training stage, volumes were randomly augmented with a 20% chance of resampling the input volume to a resolution between the native resolution and $0.8 \times 0.8 \times 2.5$ mm. Gaussian noise with a random $\sigma \in [1.0, 70.0]$ was also added during augmentation.

Training Time. Training times for each T1w autoencoder model are given below. Note that due to the time required to load and preprocess large volumetric data files, training time may vary according to the number of available CPU cores.

- Conv. LDM: 34 hours total on 4xA6000 GPUs with 48 GB of GPU memory.
- MedIL: 12 hours for pretraining and 29 hours for full autoencoder training for a total of 41 hours. MedIL was trained on 4xA6000 GPUs with 48 GB of GPU memory.
- MedIL-Interp: 12 hours for pretraining and 26 hours for full autoencoder training for a total of 38 hours. MedIL-Interp was trained on 4xA6000 with 48 GB of GPU memory.

Appendix B. Additional Reconstruction Results

We sought to understand the effect on MedIL’s performance of training on native-space data vs. fixed-size data (similar to the fully convolutional autoencoder). So, for Experiments 1 and 2, we took the MedIL weights from the pretraining stage, which were only trained on fixed-size volumes, and had MedIL reconstruct volumes in the native space. The results are shown in Table B.

Table 3: Reconstruction performance of MedIL from the pretraining stages in Experiments 1 and 2. Here, MedIL was trained on only fixed-size volumes, but evaluated on volumes in their native space.

	$\downarrow \ell_1$	\uparrow PSNR	\uparrow SSIM	\uparrow MS-SSIM	\downarrow Perceptual
<i>Experiment 1: Brain MRI</i>					
MedIL Fixed Size	0.046602	28.447635	0.831263	0.943564	0.000427
<i>Experiment 2: Lung CT</i>					
MedIL Fixed Size	0.157682	20.348748	0.613703	0.741425	0.057822